AIAA SciTech
4-8 January 2016, San Diego, California, USA
34th Wind Energy Symposium

Prediction and Analysis of the Nonsteady Transition and Separation Processes on an Oscillating Wind Turbine Airfoil using the $\gamma - Re_\theta$ Transition Model

Tarak N. Nandi* and James G. Brasseur†

Ganesh Vijayakumar*

The Pennsylvania State University, University Park, PA, 16801, United States

The present study is aimed at gaining insight into the nonsteady transitional boundary layer dynamics of wind turbine blades and the predictive capabilities of URANS based transition and turbulence models for similar physics through the analysis of a controlled flow with similar nonsteady parameters. Data extracted from CFD and BEM studies of a NREL 5MW wind turbine operating in a daytime ABL are used to estimate the nonsteady environment experienced by the blades. Data from experiments done at the University of Glasgow by Sheng et al.[1] are used to assess the ability of the $k-\omega$ SST turbulence model and the $\gamma - Re_\theta$ transition model to predict the boundary layer dynamics for the static case and for three different dynamic stall regimes likely to be experienced by wind turbine blade sections, at $Re = 1.5\times10^6$ and $M_\infty = 0.15$ using an incompressible finite volume methodology. Results from the study indicate that the $\gamma - Re_\theta$ model performs better than the SST model in capturing the static lift curve, particularly near stall. The transition model performs much better than the turbulence model in predicting the experimental hysteresis behavior for the oscillating *deep dynamic stall* case, which can be attributed to it's ability to model the laminar/transitional region near the leading edge which has a significant influence on the leading edge vortex inception and development. For the *light stall* and *stall onset* cases, where the maximum angle of attack was comparable or slightly larger than the static stall angle of attack, the transition model performs poorly, possibly due to the inability of the model to properly predict the boundary layer state near the maximum angle of attack for the oscillations.

I. Introduction

Modern commercial utility-scale wind turbines operate in the lower 10-15% of the atmospheric boundary layer (ABL), and experience temporally and spatially varying inflow from coherent ABL structures during the daytime. Lavely et al.[2] showed that the strong correlation between vertical and horizontal turbulent motions can lead to upto 50% variability in the local angle of attack (AoA or α) over a relatively short

*Graduate student, Department of Mechanical Engineering
†Professor, Department of Mechanical Engineering, Senior member

period of time around the mean at the maximum lift blade section. Nonsteadiness may also arise due to blade structural reponse to inflow, wakes from upwind turbine and yaw/pitch changes over small time scales.

The interaction of the wind turbine blades with ABL turbulence affects the temporal and spatial change in the blade boundary layer structure. In particular, the passage of coherent energetic turbulence eddies through the rotor disk can lead to large time variations in local surface stresses on the turbine blades. These blade - ABL eddy interactions underlie the observed large transients in a variety of loadings important for wind turbine functioning and reliability. The role of boundary layer transition on these transients in wind turbine loadings is not well understood. We hypothesize that laminar to turbulent blade boundary layer transition will have important effects on nonsteady blade loadings if it affects the nonsteady dynamics of boundary layer separation process on the turbine blade.

In the current study we apply unsteady Reynolds-averaged Navier-Stokes (URANS) methods to analyze boundary layer dynamics on an oscillating airfoil with large time variations in AoA in a controlled computational environment to gain insight into the nonsteady transitional boundary layer dynamics experienced by wind turbine blades in the daytime ABL

The behavior of a nonsteady boundary layer over an oscillating airfoil can be quite different from its steady/quasi-steady counterpart, the difference being a function of primarily three parameters: the mean AoA of oscillation ($\overline{\alpha}$), the amplitude of oscillation ($\Delta\alpha$) and the reduced frequency (κ) at given chord Reynolds number (Re_c). The reduced frequency $\kappa = \frac{\omega c}{2U_\infty}$ is the ratio of the convective time scale ($\frac{c}{2U_\infty}$) to the nonsteady time scale ($1/\omega$). Nonsteady aerodynamics is generally regarded as significant when κ exceeds roughly 0.05. When κ is sufficiently large, nonsteady nonlinear response may lead to hysteresis behavior in the aerodynamic force and moment values with respect to the AoA, the extent of which can vary depending on the nonsteady parameters $\overline{\alpha}$, $\Delta\alpha$and κ. Based on the combination of these nonsteady parameters, an oscillating airfoil may experience different flow regimes, ranging from little or no hysteresis behavior when the boundary layer is attached or moderately separated throughout (or for a part of) the oscillation cycle, to strong hysteresis with *deep stall* characterized by the formation and passage of strong vortical structure(s) and extensive flow separation and reattachment.[3] Prediction of this wide range of flow behavior consisting of complex separation and reattachment processes is challenging for traditional URANS based models, and the inclusion of laminar to turbulent transition only adds to this complexity.

Several researchers including McCroskey et al.,[4] McAlister et al.,[5] Leishman,[6] Martin et al.,[7] Geissler and Haselmeyer,[8] Wernert et al.,[9] Ramsay et al.,[10] Sheng et al.[1] and Lee and Gerontakos[11] have performed experiments to gain insight into the dynamics of boundary layer over airfoils in nonsteady environments. Compressibility effects start becoming important at high angles of attack when $M_\infty \geq 0.2$[12]), hence studies involving similar M_∞ are not of particular interest to us from a simulation point of view, as in the present study an incompressible Navier-Stokes solver is used.

Multiple researchers have studied numerically the influence of transition on boundary layer dynamics for static (Sorensen,[13] Langtry and Menter,[14] Counsil and Goni Boulama,[15] Rinehart et al.,[16] Brodeur and van Dam[17]) and for oscillating airfoils (Geissler and Haselmeyer,[8] Gleize et al.,[18] Wang et al.,[19] Medida and Baeder,[20] Richter et al.,[21] Vieira and Maughmer,[22] Howison and Ekici[23]) at transitional Re_c and relatively low M_∞ using various turbulence/transition modeling techniques. These studies indicate that it is challenging for a single turbulence/transition model to predict accurately the wide range of flow physics in the different dynamic stall regimes present in nonsteady environment.

In this study, data extracted from CFD (from Vijayakumar et al.[24]) and BEM (from Lavely[25]) studies of a NREL 5MW wind turbine operating in a daytime ABL are used to get an estimate of the nonsteady

environment experienced by the blades. Experimental data from Sheng et al.[1] at the University of Glasgow are used to understand the capability of the URANS based $\gamma - Re_\theta$ transition model[14] to capture important details of the dynamics of boundary layer on an S809 airfoil experiencing similar nonsteady environment. The data from the experiment are limited to only airfoil pressure measurements (alongwith the derived force and moment coefficients), so not much can be understood from these data about the state of the boundary layer accurately (particularly transition and separation locations). In this study, a deeper analysis of the nonsteady boundary layer dynamics is done through a highly resolved CFD simulation for three different cases representing the nonsteady environment felt by MW level wind turbine blade sections.

Section II provides a brief overview of dynamics and modeling of nonsteady and transitional flows. Section III gives details of the University of Glasgow wind tunnel experiments. In Section IV an estimation of the nonsteady environment experienced by various blade sections of a MW level wind turbine is done, and tests from the University of Glasgow dataset are chosen with similar nonsteady parameters. Section V give details of the computational methodology used for the simulating the flow over static and oscillating S809 airfoil, and Section VI discusses the results from the numerical study.

II. A brief overview of the dynamics and modeling of nonsteady boundary layer separation and transition for flow over an oscillating airfoil

As mentioned in the previous section, the boundary layer dynamics of an oscillating airfoil primarily depends on the mean angle of attack of oscillation ($\overline{\alpha}$), the amplitude of oscillation ($\Delta\alpha$) and the reduced frequency (κ), at a particular chord Reynolds number (Re_c). The "reduced frequency" for the pitching motion is the ratio of the free-stream convection time scale to that of the unsteady pitching motion: $\kappa = \frac{\omega c}{2U_\infty}$, and is an indicator of the extent to which flow response lags behind the pitching motion owing to inertial effects.[26] During the upstroke, the boundary layer near the leading edge between the stagnation and separation lines experiences a moving wall-jet effect (similar to that observed on a rotating cylinder),that resists separation. Also, the nonsteady Bernoulli equation applied outside the boundary layer indicates that as the airfoil pitches upwards, the adverse pressure gradient on the suction side tends to be less severe than the corresponding static case. This more favorable upstream time history of the boundary layer leads to a later separation and these factors lead to stall delay (as compared to the steady case). During the downstroke, the effects of these two factors are opposite, promoting separation (and delaying reattachment). Also, for a pitching airfoil the circulation about the airfoil changes continually with time. The velocity field associated with the shed vorticity tends to reduce the effective AoA. All these phenomena contribute to the later flow separation and delay in stall observed in the oscillating case as compared to the static case.

The $\gamma - Re_\theta$ transition model by Langtry and Menter[14] is based on the standard $k-\omega$ SST model,[27] and is suitable for implementation in a general purpose unstructured parallelized code. It is based on a combination of correlations and locally formulated transport equations. Apart from the k and ω transport equations, two other transport equations are included in the model. The first is for an "intermittency" parameter γ, that alters the production of turbulent kinetic energy term) and the second is a local parameter referred to as the "transition onset momentum thickness Reynolds number" $\widetilde{Re_{\theta t}}$, designed to take into account the variation of freestream turbulence intensity and pressure gradient. Both of these variables are defined pointwise (for computational efficiency) designed to control the production of turbulent kinetic energy term in the $k-\omega$ SST formulation. In the laminar regime, γ is forced to be zero and is gradually increased through the transition zone to a value of one in the fully turbulent region. In this model, the transition onset criterion is

based on a local parameter called "strain rate Reynolds number" $Re_v = y^2 S/\nu$, where y is the distance from the nearest wall, S is the local strain rate magnitude and ν is the kinematic viscosity. Transition is allowed when Re_v exceeds a critical value, so that transition is modeled as a local, rather than global, characteristic (for computational efficiency).

Langtry and Menter[27] modified the original $k-\omega$ SST formulation for an incompressible flow[27] as follows:

$$\frac{\partial k}{\partial t} + \frac{\partial (u_j k)}{\partial x_j} = \widetilde{P_k} - \widetilde{D_k} + \frac{\partial (\nu + \sigma_k \nu_T) \frac{\partial k}{\partial x_j}}{\partial x_j} \tag{1}$$

where $\widetilde{P_k} = \gamma_{eff} P_k$ and $\widetilde{D_k} = min(max(\gamma_{eff}, 0.1), 1.0) D_k$. P_k and D_k are the production and destruction terms in the TKE equation in the original $k-\omega$ SST equation.[27] The ω equation[27] is left intact and the blending function is changed slightly. The γ_{eff} term is mainly controlled by the transport equation for γ, which is:

$$\frac{\partial \gamma}{\partial t} + \frac{\partial (u_j \gamma)}{\partial x_j} = P_\gamma - E_\gamma + \frac{\partial (\nu + \nu_T/\sigma_f) \frac{\partial \gamma}{\partial x_j}}{\partial x_j} \tag{2}$$

where the P_γ and E_γ are source and destruction terms. The transport equation for $\widetilde{Re_{\theta t}}$ is formulated as

$$\frac{\partial \widetilde{Re_{\theta t}}}{\partial t} + \frac{\partial (u_j \widetilde{Re_{\theta t}})}{\partial x_j} = P_{\theta t} + \frac{\partial \sigma_{\theta t} (\nu + \nu_T) \frac{\partial \widetilde{Re_{\theta t}}}{\partial x_j}}{\partial x_j} \tag{3}$$

where $P_{\theta t} = \frac{c_{\theta t}}{t}(Re_{\theta t} - \widetilde{Re_{\theta t}})(1 - F_{\theta t})$, $t = 500\nu/U^2$ and $F_{\theta t}$ is a blending function which is 0 in the freestream and 1 in the boundary layer. $F_{\theta t}$ turns off the source term in the $\widetilde{Re_{\theta t}}$ equation in the boundary layer. Outside the boundary layer, $P_{\theta t}$ forces the transported scalar $\widetilde{Re_{\theta t}}$ to match the local value of $Re_{\theta t}$ calculated from empirical correlations.

As most of the correlations in this model come from numerical experiments involving flow over flat plates, the ability of the model to predict flows with high pressure gradients needs to be assessed. This model has been implemented inside the OpenFOAM[28] framework and validated for flow over a zero pressure gradient flat plate.

III. The University of Glasgow wind tunnel experiments[1]

We analyzed in detail the experiments conducted by Sheng et al.[1] in the Handley Page low-speed wind tunnel at the University of Glasgow, a closed-return tunnel with an octagonal working section of 2.13 m width and 1.61 m height. We chose these oscillating airfoils experiments because they contain a complete set of nonsteady parameter variations that surround the values experiences by utility scale wind turbine blades in the daytime atmosphere at Reynolds numbers that include boundary layer transition. The tested S809 airfoil had its trailing edge thickened for manufacturing requirements and to accommodate pressure transducers close to the trailing edge. The turbulence intensity measured at the inlet to the test section with a hot wire anemometer was approximately 1.5%. A model of the 2D airfoil with a chord length of 0.55 m and a span of 1.61 m was installed vertically in the tunnel. To reduce the three dimensional effects, care was taken to minimize the gaps between the test model and the tunnel walls. Experiments were done for static airfoils as well as airfoils with ramp-up, ramp-down and oscillating motions. For the nonsteady cases, the model was pitched about its quarter chord location by a hydraulic actuation system. 41 pressure transducers were installed at the mid-span, the measurements from which were integrated to determine the force and moment coefficients. For the oscillating airfoil tests, the pressure measurements from 10 continuous

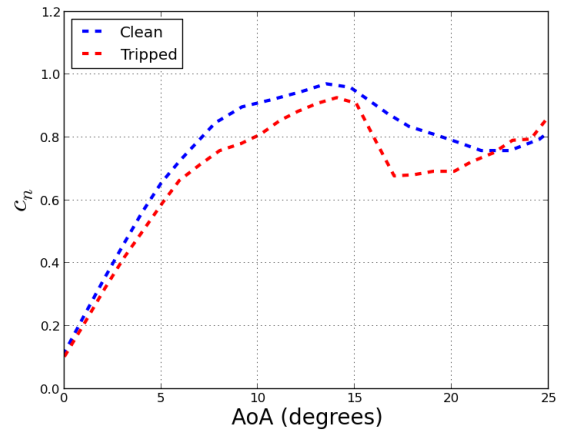

(a) Static

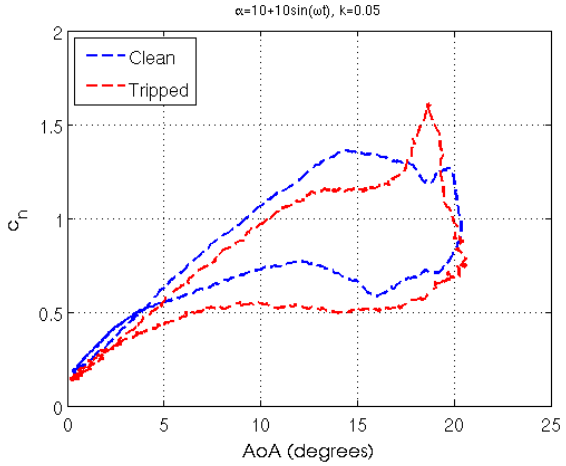

(b) Oscillating: $\overline{\alpha} = 10^0$,$\Delta\alpha = 10^0$,$\kappa = 0.05$

Figure 1: Variation of the normal force coefficient (c_n) with angle of attack (AoA) for the experimental *clean* and *tripped* (a) static cases and (b) one oscillating case (From Sheng et al.[1]).

cycles (after rejecting the initial transients) were averaged to estimate the phase-averaged force and moment coefficients.

Oscillatory tests were performed for different combinations of Reynolds number (Re), mean angle of attack ($\overline{\alpha}$), pitching amplitude ($\Delta\alpha$) and reduced frequency (κ). Experiments were carried out with and without placing roughness elements (60 grit sand strip) near the leading edge on both sides of the airfoil. In the experiments, the dynamic pressure in the test section varied over time by approximately 10% as blockage changed during oscillatory pitching of the airfoil. In the oscillating tests, although the force and moment coefficient loops showed repetitiveness from cycle to cycle for cases where the extent of hysteresis was not significant, considerable cycle to cycle variation was observed during the downstroke for the deep dynamic stall tests.

Fig. 1 shows the variation of the normal force coefficient (c_n) with angle of attack for the static cases and an oscillating case with and without leading edge roughness elements (from Sheng et al.[1]). It can be observed that for the static case, the c_n values for the clean airfoil case are higher than the tripped boundary

layer case, except near the highest AoA. Similarly, for the oscillating case, for whole of the linear part of the c_n curve, the c_n value from the clean case is higher, and the linear region extends further for the both the *clean* and *tripped* oscillating experiment compared to the corresponding static experiment because of different boundary layer improvement effects. But, near the highest AoA, a sharp rise in c_n is observed for the tripped case, indicating the presence of a leading edge vortex, whereas any such vortex if present in the clean case is much weaker (there is a relatively small rise in c_n near the highest AoA for the clean case). This observation is quite counter-intuitive from a modeling point of view, as we expect the pure turbulence models to predict poorer the leading edge instabilities (and overall flow separation) compared to a transition model hence possibly leading to an opposite trend in the prediction. The experimental observation can be possibly due to excessive thickening of the turbulent boundary layer due to the leading edge roughness elements.[29] Predicting this behavior is difficult for the URANS based models in the absence of accurate modelling of the roughness elements. Also it is interesting to observe the significant hysteresis observed in the c_n loops for the oscillating case with $\kappa = 0.05$, a value often considered to be roughly representing the onset of nonsteady aerodynamic regime.

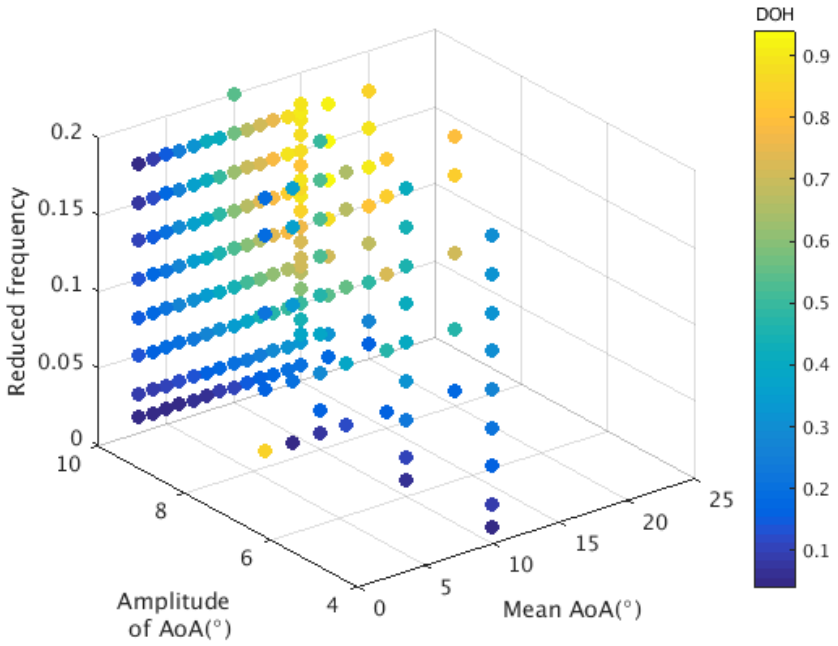

Figure 2: Variation of degree of hysteresis (DOH) with $\overline{\alpha}$, $\Delta\alpha$ and k for $Re_c = 1.5 \times 10^6$ (From experiment of Sheng et al.[1]).

IV. The Hysteresis Parameter Space (*HPS*)

We design a "Degree of Hysteresis" (*DOH*) parameter to quantify the extent of hysteresis in c_n-AoA curves. *DOH* is the difference between the normal force coefficient (c_n) during the upstroke vs. the down-stroke phase averaged over a cycle obtained from the experiment. The oscillating airfoil cases (with clean airfoil) from the University of Glasgow experiment are mapped to a *Hysteresis Parameter Space* (*HPS*) consisting of three axes: $\alpha_0, \Delta\alpha$ and κ. Each point in the *HPS* is colored by the *DOH* for a given oscillating airfoil experiment (Fig. 2). Since the aim is to understand boundary layer dynamics on airfoils experiencing

similar nonsteadiness as blade sections of utility-scale wind turbines operating in the daytime ABL, the *HPS* for a similar environment is plotted from CFD and BEM studies done in our group for a NREL 5 MW wind turbine operating in a moderately convective ABL. From the region of intersection of the 2 *HPS's* (from the University of Glasgow wind tunnel tests and the numerical study of the NREL 5MW blade), experimental cases are chosen with varying levels of *DOH* for the CFD simulations.

A blade section of a wind turbine rotor operating in the ABL experiences a combination of multiple types of nonsteady forcings (e.g. sinusoidal vertical gust, sharp-edged gust, step change in AoA), and Leishman[30] mentions that the nonsteady effects associated with these various types of motions cannot be treated by lumping them into a forcing corresponding to a net effective change in AoA. Rather, the aerodynamic response to each component of forcing must be considered separately and roughly combined through a superposition. So it should be made clear that despite our attempts, mapping a *HPS* corresponding to an oscillating airfoil using data from wind turbine inflow/aerodynamics (for a wind turbine operating in the atmosphere) data is not possible precisely. We carried out a mapping exercise none-the-less to give qualitative insight into the potential relevance of oscillating airfoil experiments to wind turbine blade boundary layer dynamics when the wind turbine blades are forced by nonsteady inflow associated with repetitive daytime atmospheric eddy passage.

To estimate the approximate combinations of nonsteady aerodynamic parameters, data from a blade boundary layer resolved CFD simulation[24] and a BEM simulation[25] of the NREL 5MW rotor rotating at 12 rpm in a moderately convective ABL with a mean wind speed of 11.5 m/s is used. Although the data from the CFD simulation are available for only 7.5 blade rotations, the BEM simulation provided data for a much longer period ($\approx$ 440 rotations) allowing us to estimate the wide range of time scales the blades encounter. From these numerical simulations, possible ranges of $\overline{\alpha}$, $\Delta\alpha$ and κ experienced by the blade sections have been estimated.

For this 5 MW wind turbine, the blade sections are cylindrical until around $r = 11.5m$ ($\approx$ 19% blade radial location), and beyond that the sections have DU and NACA airfoil profiles (see Vijayakumar et al.[24]). We searched for events in the effective AoA time history representing "large" changes in magnitude over small time scales and reaching relatively high values, as these events are likely responsible for large nonsteady forcings. To illustrate this, Fig.3 shows the variation of effective AoA and torque per unit span with time at approximately 33% radial location obtained from the CFD simulation.

The effective AoA signal in Fig.3 shows a 1-P (once-per-revolution, $5s$ for the present case) variation in amplitude. Exceptionally large changes in effective AoA can be observed from $t \approx 25s - 35s$. This type of relatively large change in effective AoA over a relatively short duration can potentially be held responsible for nonsteady blade loadings. For this particular period the minimum effective AoA (α_{min}) is around 5.5^0 and the maximum effective AoA (α_{max}) is around 18.5^0. From these values, the mean effective AoA is calculated to be approximately 12^0 ($\overline{\alpha} = (\alpha_{min} + \alpha_{max})/2$) and the amplitude is approximately 6^0 ($\Delta\alpha = (\alpha_{max} - \alpha_{min})/2$). Following a similar approach, the corresponding values of the parameters are estimated for different blade radial locations and is shown in Fig. 4.

As mentioned previously, the relatively short time duration of the CFD study precludes the possibility to estimate all the relevant time scales the wind turbine blades encounter. So, we use the BEM data of Lavely et al.[25] to plot the effective AoA spectrum (Fig. 5) for the duration of 440 blade revolutions to extract information about the different time scales which may be responsible for the nonsteady loadings. From this spectrum 3 distinct ranges of frequency can be observed:

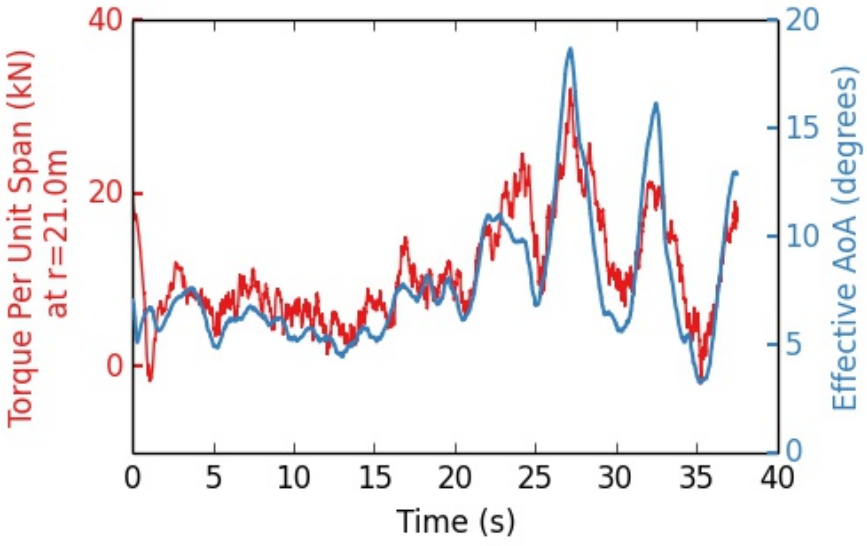

Figure 3: Variation of local effective AoA and blade torque at approximately 33% radial location from a blade boundary layer resolved CFD simulation of the NREL 5MW blade in daytime ABL (from Vijayakumar et al.[24]).

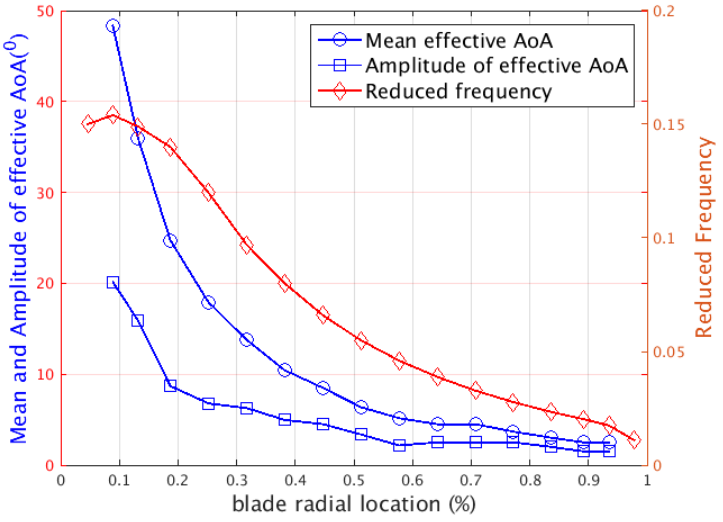

Figure 4: Variation of mean and amplitude of effective angle of attack and reduced frequency at various radial locations of the NREL 5MW blade.

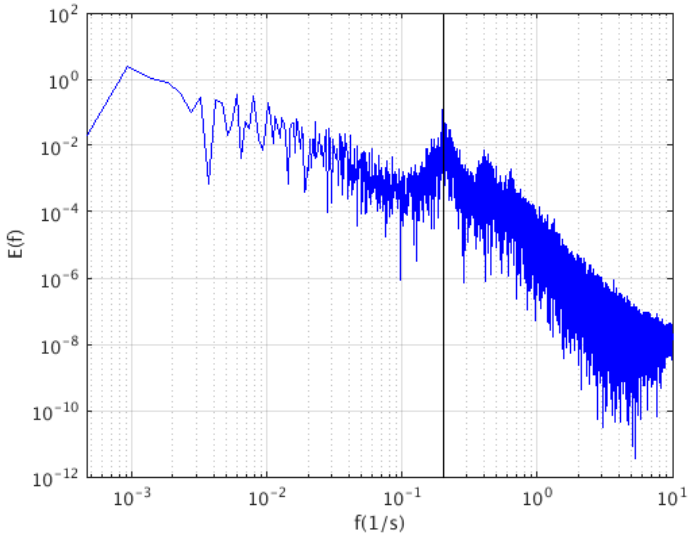

Figure 5: Energy spectrum for effective AoA from the BEM simulation of the NREL 5MW rotor in daytime ABL (from Lavely[25]). The convection frequency is shown by the vertical black line.

1. the low frequency time scales corresponding to quasi stationary weather changes and eddy passage (frequency, $f < 0.1s^{-1}$)
2. 1-P time scale (blade rotation time scale corresponding to $f = 0.2s^{-1}$)
3. sub 1-P time scale ($f > 0.2s^{-1}$).

The most prominent peak in the spectrum by far is at the 1-P frequency corresponding to the blade rotation time ($f = 0.2s^{-1}$). Therefore, we use the blade rotation time as the dominant nonsteady time scale. Based on the 1-P frequency (and the local inflow speed), the reduced frequency estimates for different blade sections is shown in Fig.4. If it were assumed that nonsteady aerodynamics is important for reduced frequencies larger than 0.05, it can be observed that for the $5s$ time scale (representing the blade rotation time scale), the blade sections from the root to around 50% span experience nonsteady aerodynamics.

Table 1: Nonsteady parameters associated with the nonsteady loadings of the NREL 5MW blade sections from CFD[24] (labeled "5 MW") and the corresponding cases from the Glasgow dataset[1](labeled "expt").

r/R	$\overline{\alpha_{5MW}}$	$\Delta\alpha_{5MW}$	κ_{5MW}	Glasgow case no.	$\overline{\alpha_{expt}}$	$\Delta\alpha_{expt}$	κ_{expt}
0.252	17.9	6.78	0.12	5104	15	10	0.1
0.317	13.78	6.27	0.097	5161	12	8	0.1
0.382	10.43	4.97	0.08	5014	10	6	0.072

Fig. 6 shows the subset of the *HPS* extracted from the above study using the CFD and BEM studies of the NREL 5MW blade for 1-P time scale. From the study of the *HPS* spanned by the various blade sections, the sections at $r/R = 0.252$, 0.317 and 0.382 are chosen to be representative of wind turbine blade sections

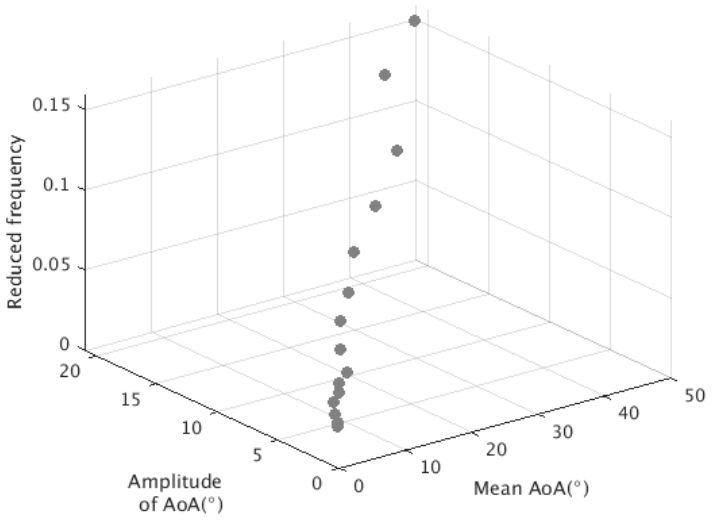

Figure 6: HPS extracted from the CFD simulation of the NREL 5MW single bladed rotor for 1-P time scale.

experiencing nonsteady aerodynamics, and the Glasgow database is searched to look for cases having similar combination of nonsteady parameters. The nonsteady parameters for these cases and the experimental cases representative of quite similar nonsteady environment are listed in Table 1. The blade sections from the root to $\approx 25\%$ radial location are very thick (as compared to the 21% thick S809 airfoil) and hence haven't been listed (although they do experience significant nonsteadiness). For $r/R > 0.382$, the corresponding DOH estimated from the Glasgow experiments are relatively small. The following sections give details about the numerical study of the steady as well as the above mentioned oscillating S809 cases.

V. Computational Methodology

The computational domain created is a close two dimensional replica of the experimental test section. The airfoil chord and the distance from the airfoil to the inlet and the tunnel walls in the computational domain are kept the same as that of the experiment. An O-grid is created with a circular interface approximately 1.5 chord away from the airfoil quarter chord location to allow the oscillation of the airfoil, and the interpolation of the data between the oscillating mesh and the static mesh is done using the "Arbitrary Mesh Interface" (AMI) capability in OpenFOAM. A schematic of the domain with the relevant dimensions is shown in Fig. 7.

The inlet velocity (U_{in}) and turbulence intensity (Tu_{in}) are prescribed according to the experimental conditions. Using these quantities, the turbulent kinetic energy at the inlet (k_{in}) is prescribed according to $k_{in} = 1.5(U_{in}Tu_{in})^2$. The inlet turbulent Reynolds number (ratio of the freestream turbulent viscosity to molecular viscosity) is appropriately chosen to capture the free decay of turbulent kinetic energy (k) from the inlet to the airfoil. Based on k_{in} and the turbulent Reynolds number, a parameter representing inverse eddy time scale at the inlet (ω_{in}) is calculated from $\omega_{in} = k_{in}/\nu_t$. The $\gamma - Re_\theta$ model requires γ to have a fixed value of 1 at the inlet and $\widetilde{Re_{\theta t}}$ be calculated from correlations prescribed in the model. At the outlet, pressure is prescribed as constant, and zero gradient boundary conditions are applied for other variables. At the airfoil surface, no-slip boundary condition is applied with k set to zero. The value of ω at the airfoil

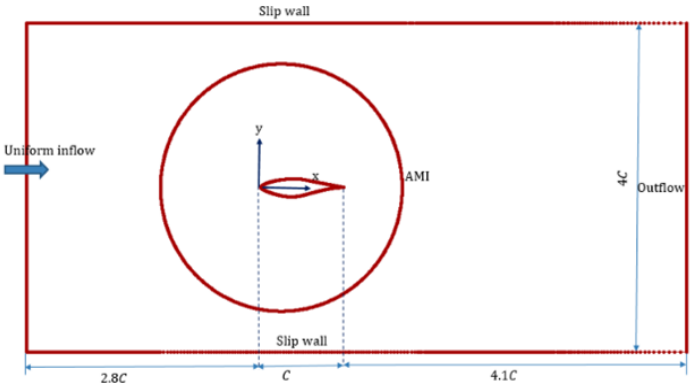

Figure 7: Schematic of the computational domain.

surface is prescribed using the relation[27] $\omega_{wall} = 60\nu/\beta_1 y_1^2$, where ν is the molecular viscosity, $\beta_1 = 0.075$ and y_1 is the distance of from the wall to the the center of the first layer of cells off the wall. Zero gradient boundary conditions are applied for γ and Re_θ at the airfoil surface.

A SIMPLE-based transient solver capable of handling moving meshes is used for the Navier Stokes equations and the transport equations for the transition/turbulence variables. The convective terms in the discretized transport equations (written as the divergence of a flux term in the finite-volume methodology) are approximated using the 2^{nd} order linear upwind scheme, and time-stepping is done using a 2^{nd} order scheme. The pressure Poisson equation is solved using a Preconditioned Conjugate Gradient (PCG) solver with a Diagonal Incomplete Cholesky (DIC) preconditioner. The linearized equations for the other variables are solved using the Preconditioned Biconjugate Gradient (PBiCG) solver with a Diagonal Incomplete LU (DILU) preconditioner. The mean Courant number in the domain is maintained below 0.1 using adaptive time stepping, and the highly resolved near-wall region mesh ensured $y^+ < 1$ at the first grid level off the airfoil surface.

A study was done to check the sensitivity of the static and oscillating simulations to the grid using the $\gamma - Re_\theta$ transition model (more sensitive to the mesh resolution than the SST turbulence model) resulting in a baseline O-grid (G_1) with 478 cells around the airfoil with 80×130 cells in the wake region and two other refined grids, one with 877 cells around the airfoil and 150×230 cells in the wake region (G_2) and another with 1774 cells around the airfoil with 300×450 cells in the wake region (G_3). These three grids were used for studying the flow at static AoA's of 10^0 (flow with little or no separation) and 16^0 (flow with significant separation), and for one oscillating *light stall* case. The difference in c_l and c_d were less than 2% and 3% respectively for the static cases using the 3 grids, and G_1 was used for the static airfoil simulations. For the oscillating case, the leading edge resolution of G_1 was found to be inadequate, whereas the maximum difference in c_l and c_d are not more than 5% when G_2 and G_3 are used. Hence G_2 was used for the oscillating airfoil simulations.

VI. Results and Discussions

A. Static airfoil

Simulations for the static airfoil were carried out using the $\gamma - Re_\theta$ transition model and the SST turbulence model for angles of attack from $0^0 - 20^0$ for $Re_c = 1.5 \times 10^6$. Comparison of the numerical predictions is done with experimental datasets from three sources: University of Glasgow,[31] The Ohio State University,[10] and Delft University of Technology.[29] During these test campaigns, experiments were carried out for flow over clean S809 airfoil as well as with leading edge roughness elements (hereafter referred to as the *clean* airfoil and the *tripped* airfoil respectively) to force transition of the boundary layer.

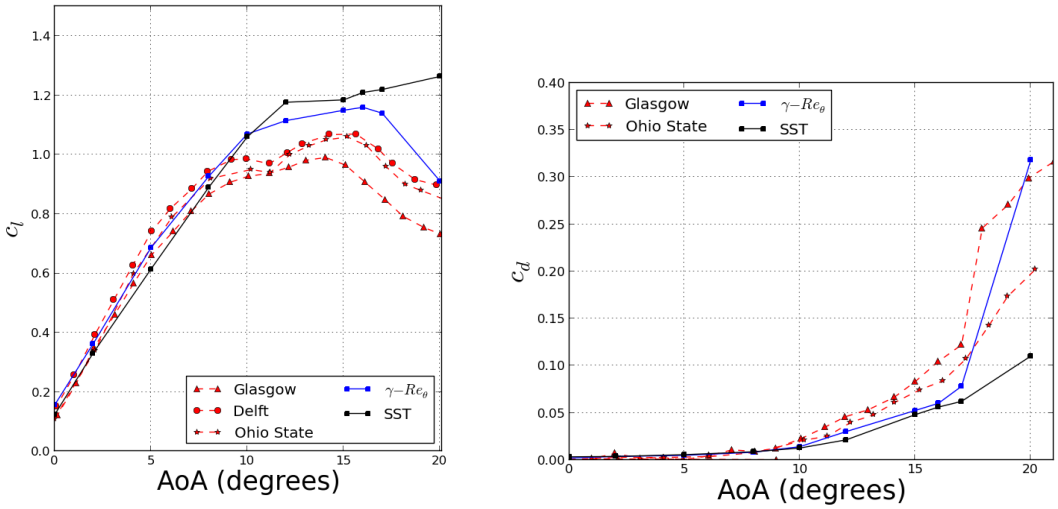

(a) Coefficient of lift (c_l)

(b) Coefficient of drag (c_d)

Figure 8: Comparison of lift and pressure drag coefficient predictions with *clean* airfoil data.

The transition model is designed to predict laminar, transitional and the fully turbulent flow regimes for the flow over the *clean* airfoil. However for the *tripped* airfoil, the dependence of the boundary layer evolution on the details of the roughness elements cannot be captured by the SST model. In the present work, both models are applied to the effectively *clean* airfoil cases, which may be representative of wind turbine blade sections without significant leading edge contaminations.

1. *Comparison of integrated force coefficients with the fully turbulent (SST) and transition ($\gamma - Re_\theta$) models with* clean *airfoil data*

Fig. 8 shows the comparison of the numerical predictions of the lift and pressure drag coefficients (c_l and c_d) vs. angle of attack with the corresponding experimental values for the *clean* airfoil cases. The numerical predictions and the datasets as well as the datasets among themselves are reasonably close to one another for $\alpha \lesssim 10^0$, likely where little or no trailing edge separation is present. However significant deviations are observed at higher AoA's. The differences between the experimental datasets at the higher AoA's can likely be attributed to tunnel interference effects, differences in freestream turbulence intensity and differences in aspect ratio of the test wings. In Fig. 8(b), we compare pressure drag coefficient only with the Ohio State and University of Glasgow data because the data from Delft University provide only the total drag coefficient.

Fig. 8 shows that while the $\gamma - Re_\theta$ transition model predicts the experimental trends in the behavior of the force coefficients near and beyond the stall angle, the corresponding predictions from the SST model are relatively poor. The inability of the RANS based turbulence models to predict the flow behavior near and beyond stall is a well known phenomenon.[32]

From the University of Glasgow dataset (Fig. 1) it can be observed that the normal force coefficient c_n for the *clean* cases are higher than the *tripped* cases from the lowest AoA (-2^0) to AoA's much beyond the static stall AoA. However, for the CFD simulations (Fig. 8(a)), it can be observed that while the predicted c_l values are higher with the $\gamma - Re_\theta$ transition model relative to the SST model when $\alpha \lesssim 10^0$, the trend is reversed beyond that. The trend in the lower AoA regime ($\lesssim 10^0$ observed in both the CFD simulations and the experiments) is possibly due to the higher viscous decambering of the S809 airfoil by the thicker turbulent boundary layer.[29] For AoA sufficiently large that trailing edge separation is prominent, it is expected that the SST model would predict higher c_l than the $\gamma - Re_\theta$ transition model due to higher momentum diffusivity with corresponding greater ability to resist separation. This is observed in the CFD predictions. However the corresponding trend is opposite in the experimental datasets, possibly due to the excessive thickening of the boundary layer by the leading edge roughness elements.[29]

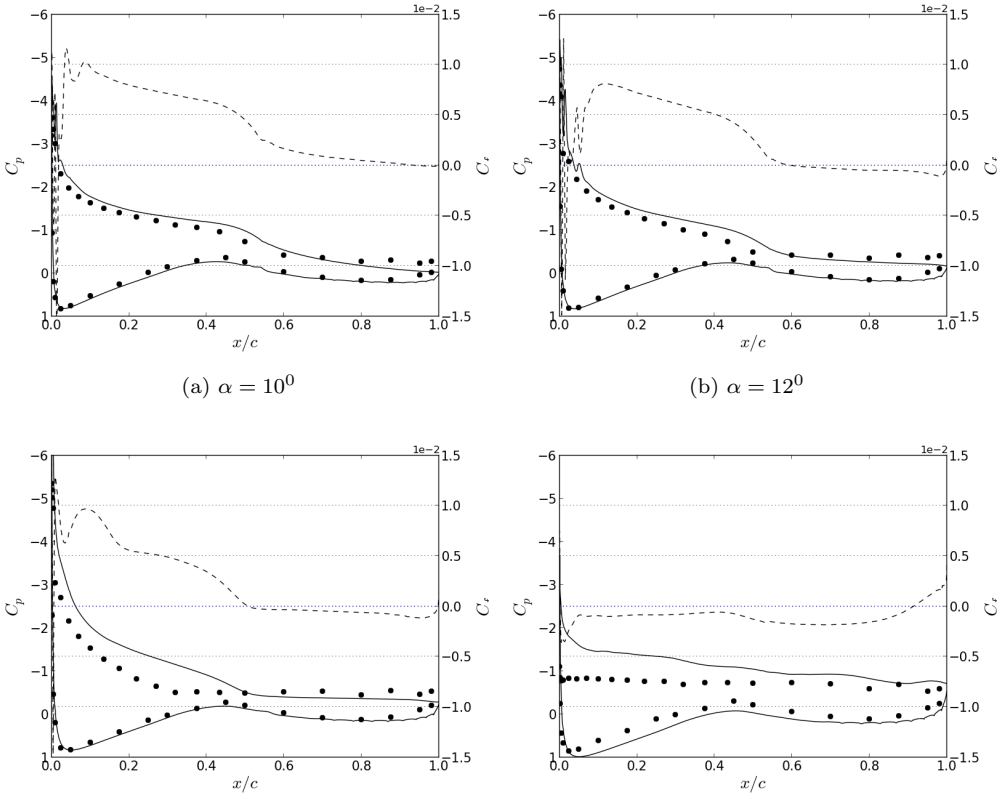

(a) $\alpha = 10^0$ (b) $\alpha = 12^0$

(c) $\alpha = 15^0$ (d) $\alpha = 20^0$

Figure 9: Chordwise coefficient of pressure (C_p) and skin friction coefficient (C_f) variation using the $\gamma - Re_\theta$ transition model for angles of attack of (a) 10^0, (b) 12^0, (c) 15^0 and (d) 20^0. Black dots: Experimental C_p, Black solid line: C_p from simulation, Black dashed line: C_f from simulation (on the suction side).

Figs. 9 and 10 compare pressure coefficient (C_p) distribution predictions with the $\gamma - Re_\theta$ transition model and the the SST turbulence model respectively for the *clean* cases in the experiment. While trailing

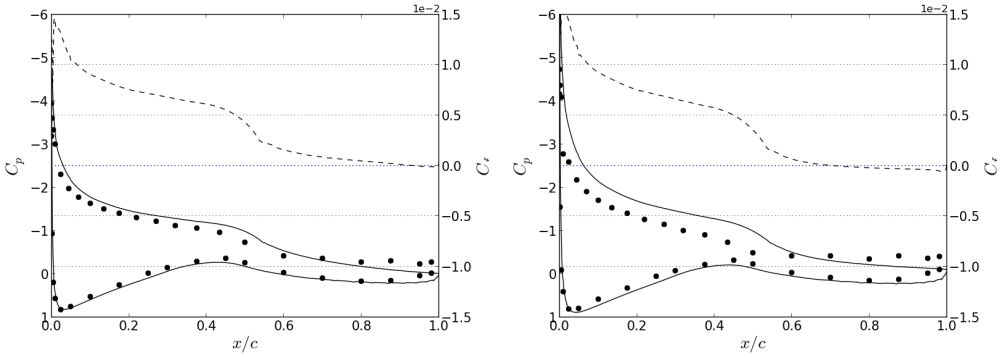

(a) $\alpha = 10^0$

(b) $\alpha = 12^0$

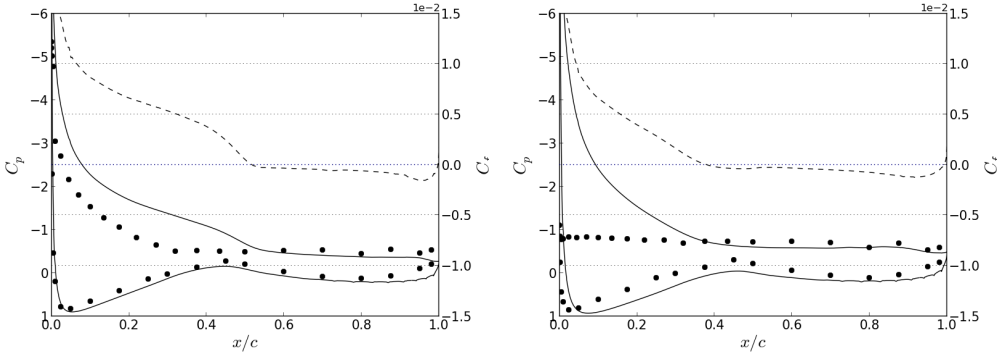

(c) $\alpha = 15^0$

(d) $\alpha = 20^0$

Figure 10: Chordwise coefficient of pressure (C_p) and skin friction coefficient (C_f) variation using the SST turbulence model for angles of attack of (a) 10^0, (b) 12^0, (c) 15^0 and (d) 20^0. Black dots: Experimental C_p, Black solid line: C_p from simulation, Black dashed line: C_f from simulation (on the suction side).

edge separation is apparent at $\alpha = 10^0$ in the experiment (inferred from the relatively flat C_p profile near the trailing edge), separation occurs when $\alpha \gtrsim 12^0$ in the numerical simulations (confirmed by the C_f plots). This delay in separation prediction is manifested in the higher c_l prediction by the transition and turbulence models as compared to the experiment. For $\alpha = 12^0$, the extent of trailing edge separation is slightly greater in the transition model prediction, leading to a lower c_l compared to the SST model prediction. It can be observed that at $\alpha = 20^0$ the experimental data for both *clean* and *tripped* cases show massive separation on the suction side right from near the leading edge. The $\gamma - Re_\theta$ transition model predicts this behavior but the SST model does not; the SST model predicts $\approx 40\%$ attached flow on the suction side at this AoA. It is to be noted that the pressure coefficient is slightly different from one at the stagnation point because some adjustments were done to the experimental data to the expression of C_p, and a similar adjustment is done to the the numerical data too.

Also at lower AoA's, both the transition and turbulence models predict the pressure drag relatively well, whereas at higher AoA's, the greater amount of separation predicted by the transition model leads to a sharp increase in c_d consistent with the experimental observations (Fig. 8(b)).

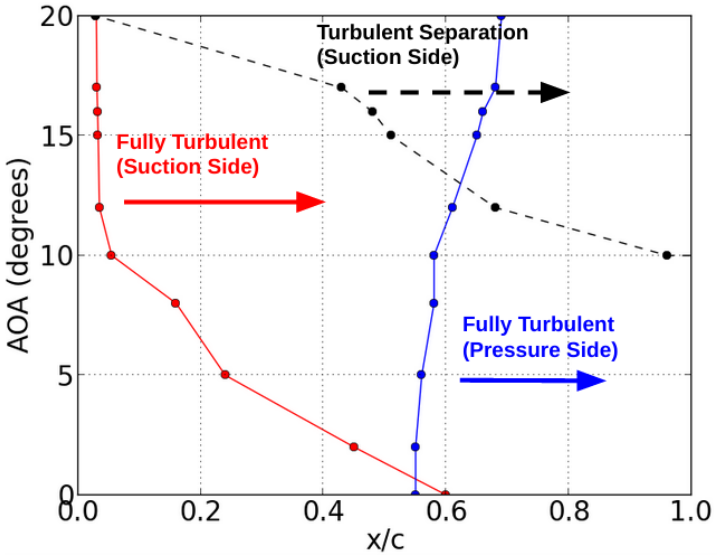

Figure 11: Variation of the extent of turbulent flow and separated flow with angle of attack for the static cases using the $\gamma - Re_\theta$ transition model.

2. Variation of the extent of turbulent flow and separated flow with angle of attack

Fig. 11 shows the variation of the extent of turbulent flow and separated flow with AoA predicted with the $\gamma - Re_\theta$ transition model simulations. No noticable turbulent flow separation is predicted on either side of the airfoil below $\alpha \approx 12^0$, whereas beyond this angle trailing edge flow separation is observed on the suction side and the separation location moves rapidly towards the leading edge with increasing AoA. No turbulent flow separation is predicted on the pressure side at any of the AoA. At $\alpha = 0^0$ only the last $\approx 40\%$ of the boundary layer on either side is predicted to be fully turbulent. With increasing AoA, the extent of fully turbulent region on the suction side increases gradually and reaches the leading edge region at an approximate AoA of 12^0 whereas the extent of the fully turbulent region on the pressure side decreases slightly with increasing AoA.

B. Oscillating airfoil

1. Airfoil oscillating well beyond static stall angle of attack: $\alpha(t) = 15^0 + 10^0 sin(\omega t)$, $\kappa = 0.1$

The dynamic stall regime, where the airfoil motion far exceeds the static stall AoA is characterized by the formation of a leading edge vortex, and is referred to as *deep dynamic stall*. This regime is associated with large nonsteady aerodynamic loads accompanied by significant extent of hysteresis behavior.

(a) **Comparison of the $\gamma - Re_\theta$ transition model predictions with the *clean* airfoil experiment.**

Fig.12 shows the comparison of the variation of the phase averaged lift, drag and moment coefficients (averaged over four cycles after rejecting the first two cycles representing the initial transients) with angle of attack from the the $\gamma - Re_\theta$ transition model simulation with the experiment using *clean* airfoil undergoing *deep dynamic stall*. The numerical predictions agree well with the experiment during the upstroke part of the cycle until $\alpha \approx 15^0$. However the linear increase in c_l continues for approximately

2.5^0 beyond the corresponding experimental value. This prediction is consistent with the spurious delay in stall prediction in the static case (Fig. 8(a)).

The prediction of the subsequent sharp increase in c_l, which can be attributed to the increased suction due to the development of the leading edge vortex, is also delayed slightly. The formation and passage of the vortex along the airfoil surface also leads to a sharp increase in pressure drag. The decrease in c_l near the maximum angle of attack is due to the detachment of the leading edge vortex from the airfoil surface, and the aftward movement of the vortex leads to a large nose-down pitching moment (Fig. 12(c)). Both of these events are predicted approximately 2^0 later than the experiment. During the downstroke, the boundary layer on the suction side undergoes reattachment and relaminarization, the highly nonsteady and stochastic nature of which lead to the fluctuating nature of the force and moment coefficients. The error bars in Fig. 12 give an indication of the cycle to cycle variation of c_l during the downstroke observed both in the experiment and the simulation. No such estimates of cycle-to-cycle variation are available for the experimental drag and moment coefficients.

(b) **Deeper understanding of the *deep dynamic stall* process and the variation of transition and separation location with angle of attack**

The rapid pitch-up motion of the airfoil maintains a strong favorable pressure gradient near the leading edge. This is evident from the large leading edge suction peaks in Fig. 13, which shows the variation of the pressure coeffcient C_p along the airfoil surface during a part of the upstroke, which significantly enhances production of vorticity in the region near the leading edge. The concentration of vorticity near the leading edge grows with increase in angle of attack, and leads to the formation of the leading edge vortex, the influence of which can be observed from the sharp increase in lift and drag coefficients (Figs. 12(a) and 12(b)). The formation, detachment and the passage of the leading edge vortex over the airfoil can observed from the vorticity isocontours (Fig. 14) at angles of attack of 22^0, 23^0, 24^0 and 25^0 during the upstroke. The formation of the leading edge vortex can be identified from the region of strong clockwise vorticity near the leading edge (Fig.14(b)) As the leading edge vortex evolves, a vortex induced separated region due to the strong local adverse pressure gradient is observed beneath, leading to the development of a secondary vortex (Fig. 14(c))with opposite signed vorticity.

The leading edge vortex attains its peak strength at $\alpha \approx 24^0$ and contributes significantly to the maximum lift observed in the cycle, which is more than 50% higher than the maximum static lift value. The vortex detached from the surface convects over the suction surface before being shed into the wake (Fig. 14(d)). The influence of the dynamics of this vortex on the pressure drag and the pitching moment can be observed in Figs. 12(b) and 12(c). The formation and subsequent growth of the leading edge vortex results in a sharp increase in the pressure drag and its movement towards the trailing edge causes the suction peak to move aftward too (Fig. 13), leading to large nose-down pitching moment (Fig. 12(c)). The maximum lift and drag force coefficients and the maximum negative pitching moment value obtained from the simulations are in good agreement with the experiment, but occur at relatively later angles of attack. It is observed that although the moment coefficient loop obtained from the experiment is counterclockwise throughout, the transition model predicts a small clockwise loop during the downstroke part which indicates negative aerodynamic damping and may have an influence on stall flutter predictions.

A sudden rise in c_l is observed during the initial portion of the downstroke, which can be tied to the formation of a relatively large trailing edge vortex. Thereafter, c_l starts to drop but large fluctuations

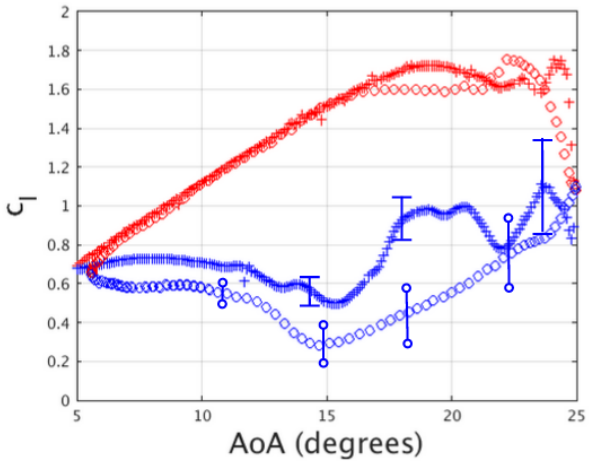

(a) Coefficient of lift (c_l)

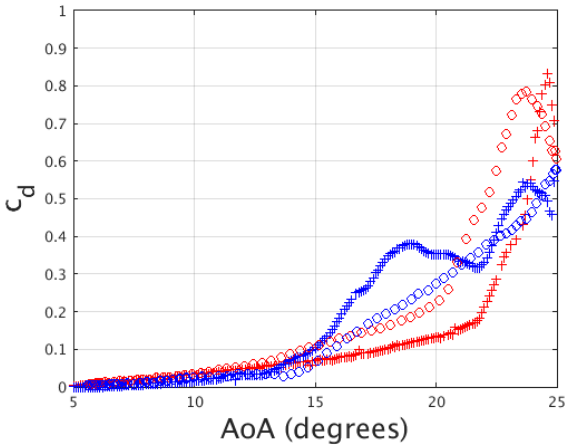

(b) Coefficient of drag (c_d)

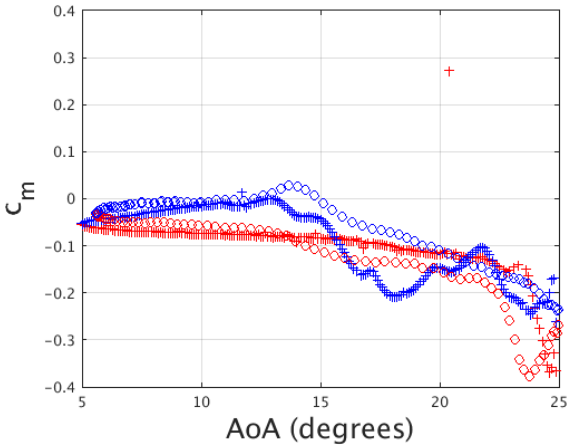

(c) Coefficient of moment (c_m)

Figure 12: Variation of lift, drag and moment coefficient predictions with AoA for $\alpha(t) = 15^0 + 10^0 sin(\omega t)$, $\kappa = 0.1$, using the $\gamma - Re_\theta$ transition model. Red Cross: Transition model-Upstroke, Blue cross: Transition model-downstroke, Red circles: Experiment-upstroke, Blue circles: Experiment-downstroke.

are observed in the profile, mainly due to the occurrence of nonsteady separation/reattachment processes (Fig. 15(b)). Reattachment over a large section of the suction side completes at $\alpha \approx 13^0$ (Fig. 15(b)), after which c_l starts increasing continually till the minimum AoA is reached.

Fig. 15 shows the extent of fully turbulent and separated regions on the airfoil surface(s) during one complete cycle. At the lowest AoA during the upstroke, no turbulent flow separation is observed and approximately 40% of both the surfaces is fully turbulent. With increasing AoA, while the extent of turbulent flow region increases rapidly on the suction side, it gradually decreases on the pressure side. At $\alpha \approx 13^0$, almost the whole of the the suction side is predicted to be fully turbulent. While almost whole the of the pressure side is laminar at the end of the upstroke. During the downstroke, rapid reattachment takes place on the suction side with fully attached flow as the airfoil crosses $\alpha \approx 13^0$. Also parts of the boundary layer return to the laminar state with decreasing AoA, and by the time the airfoil reaches the lowest AoA, laminar flow extends for more than half of the suction side. No turbulent flow separation is

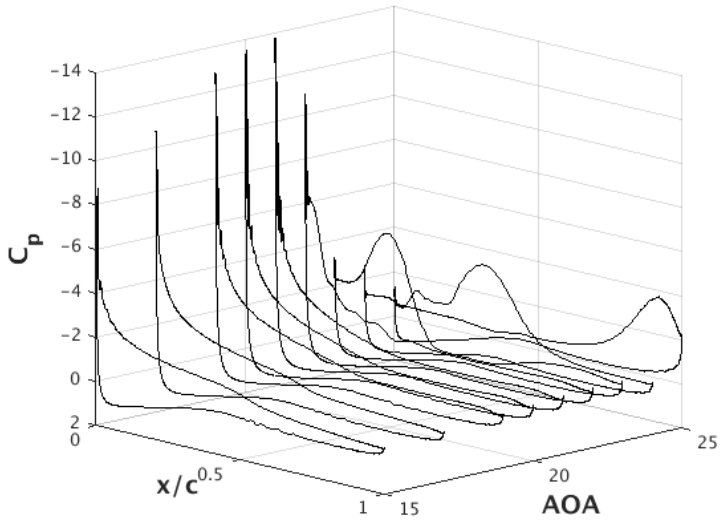

Figure 13: C_p variation during the upstroke for one particular cycle from the $\gamma - Re_\theta$ transition model simulation for $\alpha(t) = 15^0 + 10^0 sin(\omega t)$, $\kappa = 0.1$.

predicted on the pressure side at any AoA, although laminar separation bubbles are predictedd which are responsible for the transition process.

(c) **Comparison of the SST turbulence model predictions with the *clean* airfoil experiment**

Fig. 16 shows that the SST turbulence model predictions of the force and moment coefficients are much poorer than those from the $\gamma - Re_\theta$ transition model, with significant delay in the prediction of the formation of the leading edge vortex, accompanied by delayed increase in the lift and drag coefficients and the nose-down pitching moment. The leading edge vortex formation is predicted to initiate very close to the maximum AoA and does not form completely, leading to a relatively different boundary layer behavior during the downstroke than predicted with the transition model. The prediction of the overall extent of hysteresis (DOH) is lower than the corresponding $\gamma - Re_\theta$ transition model prediction. This relatively poor prediction of the hysteresis behavior can be tied to the under-prediction of separated flow near and beyond stall in the static cases.

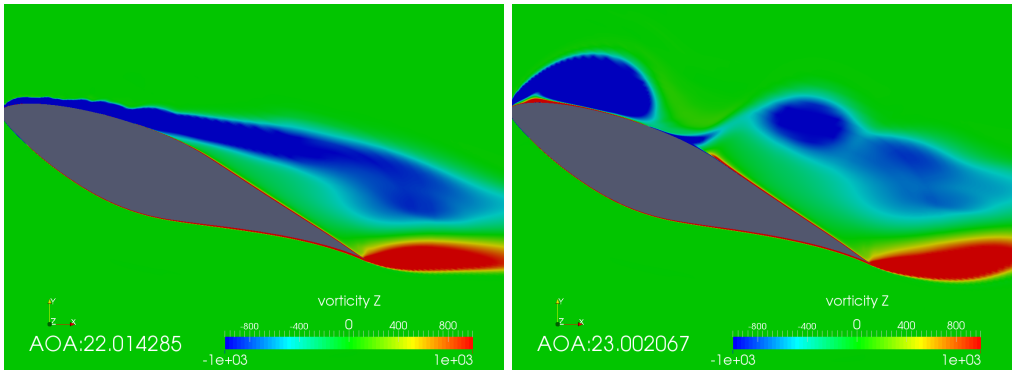

(a) $\alpha \approx 22^0 \uparrow$ (b) $\alpha \approx 23^0 \uparrow$

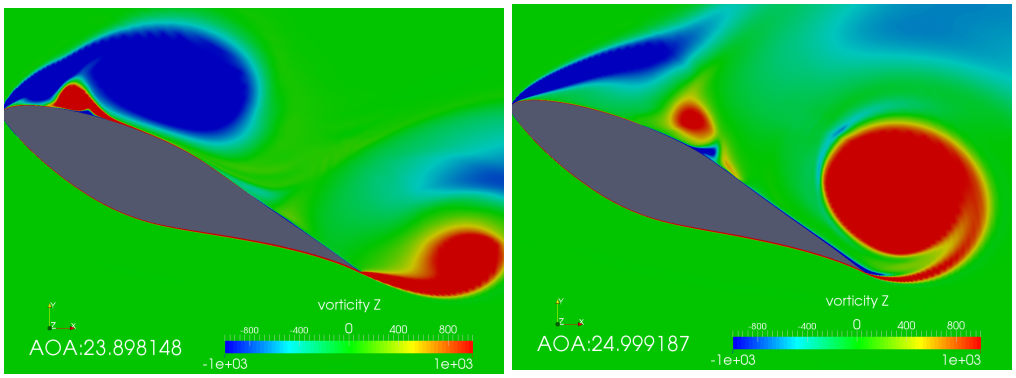

(c) $\alpha \approx 24^0 \uparrow$ (d) $\alpha \approx 25^0$

Figure 14: Spanwise vorticity magnitude (s^{-1}) isocontours during the upstroke for angles of attack of (a) 22^0 , (b) 23^0, (c) 24^0 and (d) 25^0 for $\alpha(t) = 15^0 + 10^0 sin(\omega t)$, $\kappa = 0.1$, using the $\gamma - Re_\theta$ transition model.

(d) **Reasoning behind the requirement for the transition model to better predict the experimental hysteresis behavior**

It is observed that the transition model performs better than the SST turbulence model in predicting the experimental boundary layer events, and consequently the overall hysteresis behavior for the *deep stall* case discussed above. This can be attributed to the better prediction of boundary layer instabilities originating near the leading edge near the maximum angle of attack, which are favored by the prediction of the laminar region near the leading edge. Fig. 17 shows the isocontours of turbulent kinetic energy near the leading edge at $\alpha \approx 21^0$, from the transition model and the turbulence model predictions. It can be observed that laminar flow exists from the stagnation point to approximately 3% of the suction side in the transition model prediction, whereas the usage of the SST model leads to high turbulent kinetic energy right from the leading edge making the boundary layer much less prone to instabilities than the transitional boundary layer. These instabilities ultimately lead to the formation of the leading edge vortex, which has a significant impact on the overall hysteresis behavior.

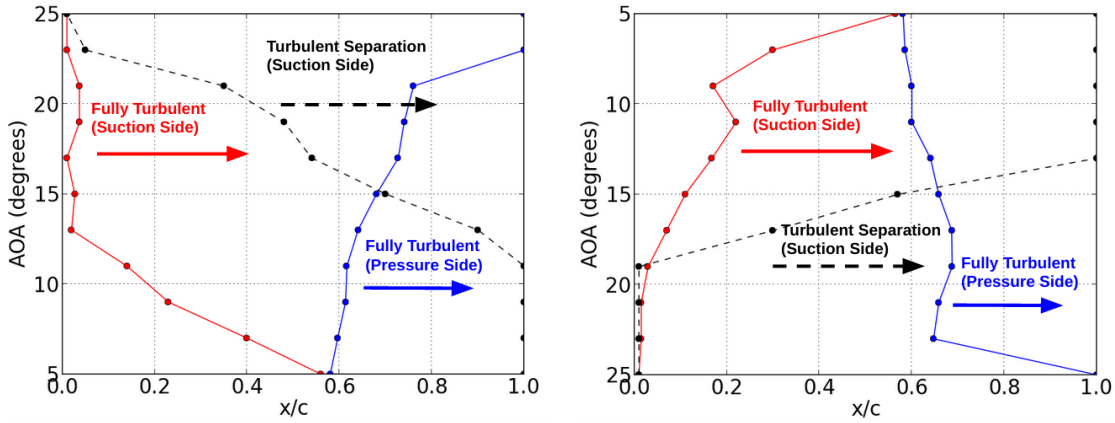

(a) Upstroke

(b) Downstroke

Figure 15: Variation of the extent of turbulent flow and separated flow with angle of attack for $\alpha(t) = 15^0 + 10^0 sin(\omega t)$, $\kappa = 0.1$, using the $\gamma - Re_\theta$ transition model.

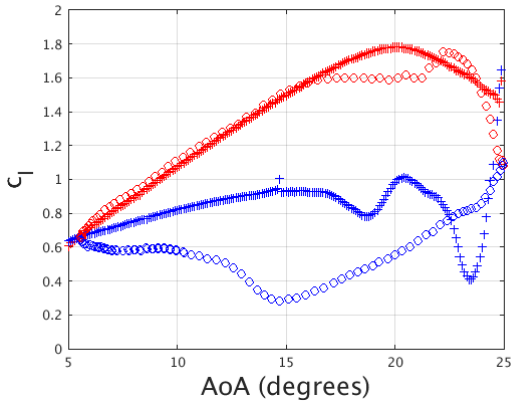

(c) Coefficient of lift (c_l)

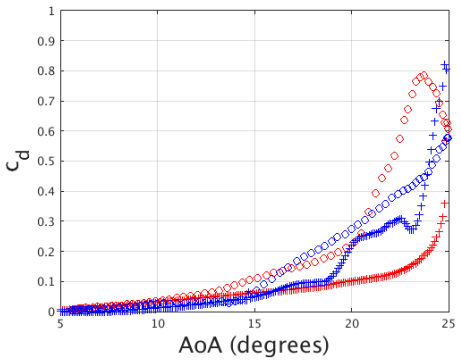

(d) Coefficient of drag (c_d)

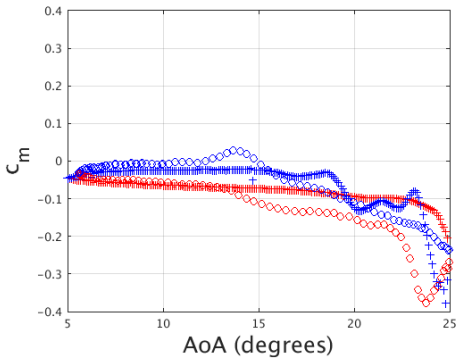

(e) Coefficient of moment (c_m)

Figure 16: Variation of lift, drag and moment coefficient predictions with AoA for $\alpha(t) = 15^0 + 10^0 sin(\omega t)$, $\kappa = 0.1$, using the SST turbulence model. Red Cross: Transition model-Upstroke, Blue cross: Transition model-downstroke, Red circles: Experiment-upstroke, Blue circles: Experiment-downstroke.

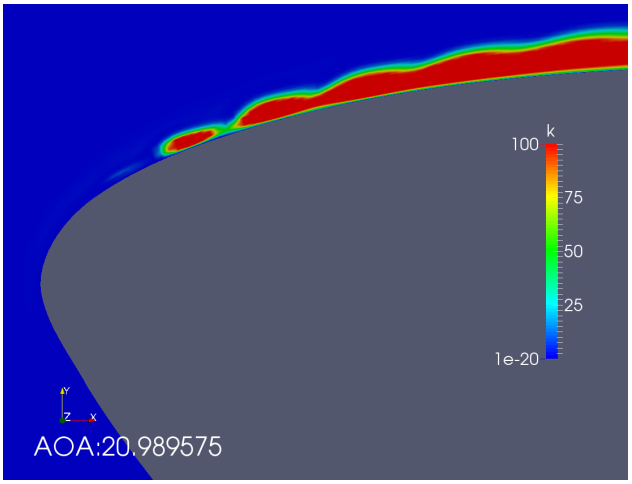

(a) $\gamma - Re_\theta$ transition model

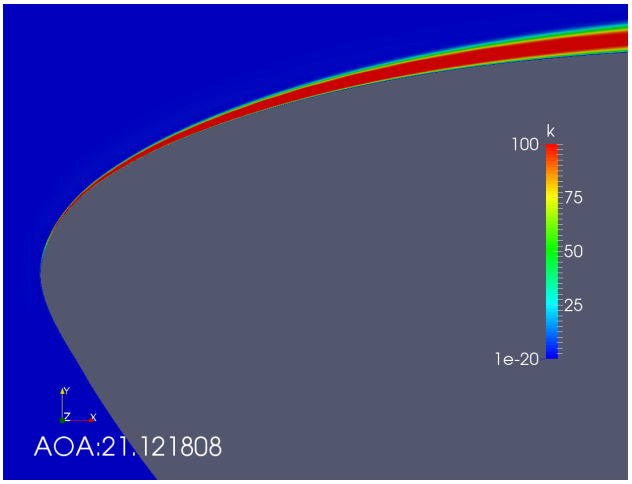

(b) SST turbulence model

Figure 17: Turbulent kinetic energy isocontours (in m^2/s^2) near the leading edge at $\alpha \approx 21^0$ upstroke using the (a) $\gamma - Re_\theta$ transition model and (b) SST turbulence model (for $\alpha(t) = 15^0 + 10^0 sin(\omega t)$, $\kappa = 0.1$).

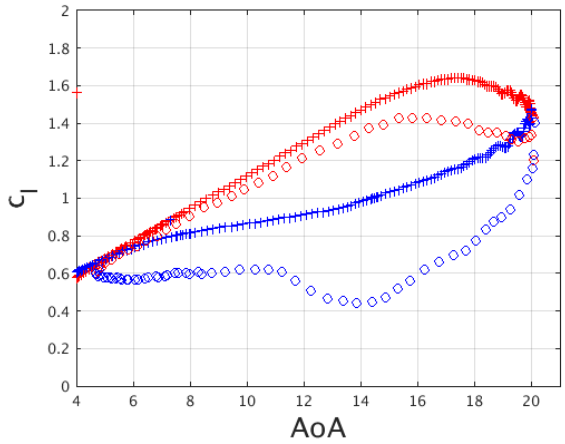

(c) Coefficient of lift (c_l)

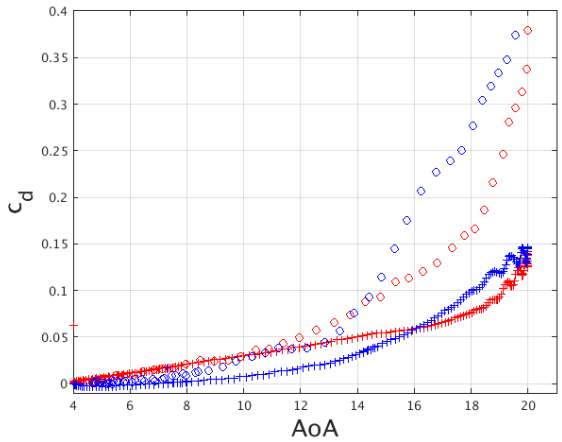

(d) Coefficient of drag (c_d)

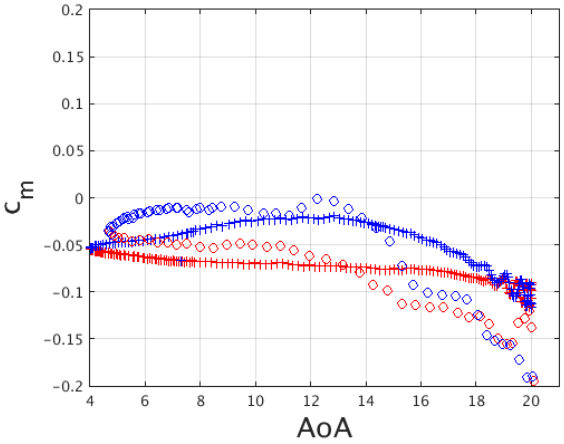

(e) Coefficient of drag (c_m)

Figure 18: Variation of lift, drag and moment coefficient predictions with AoA for $\alpha(t) = 12^0 + 8^0 sin(\omega t)$, $\kappa = 0.1$, using the $\gamma - Re_\theta$ turbulence model. Red Cross: Transition model-Upstroke, Blue cross: Transition model-downstroke, Red circles: Experiment-upstroke, Blue circles: Experiment-downstroke.

2. Maximum AoA comparable or slightly larger than the static stall AoA:
$\alpha(t) = 12^0 + 8^0 sin(\omega t)$, $\kappa = 0.1$ and $\alpha(t) = 10^0 + 6^0 sin(\omega t)$, $\kappa = 0.072$

Cases where the maximum AoA reached by the airfoil is comparable or slightly larger than the static stall AoA are referred to as *stall onset* and *light stall* respectively. These flows do not allow the complete formation of the leading edge vortex or suppresses it completely, leading to much less flow separation and hysteresis behavior compared to *deep stall*. Because of the relatively poor performance of the SST turbulence model for *deep stall*, this model was not applied to these two cases. Although the transition model predicts reasonably well the boundary layer dynamics for *deep stall*, it's ability to predict *stall onset* and *light stall* is of interest too.

(a) **Comparison of the $\gamma - Re_\theta$ transition model predictions with the *clean* airfoil experiments**

Fig. 18 shows the comparison of the force and moment coefficients from the $\gamma - Re_\theta$ transition model

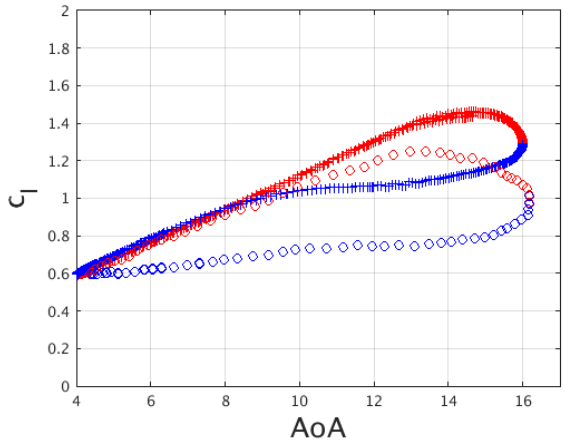

(a) Coefficient of lift (c_l)

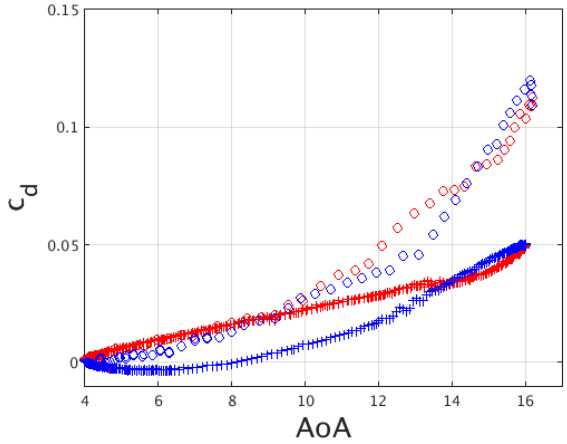

(b) Coefficient of drag (c_d)

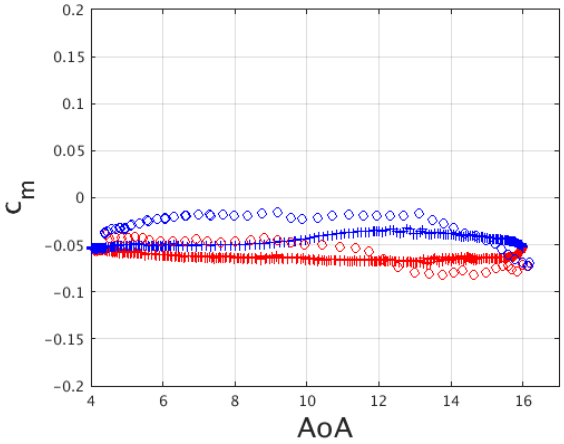

(c) Coefficient of moment (c_m)

Figure 19: Variation of lift, drag and moment coefficient predictions with AoA for $\alpha(t) = 10^0 + 6^0 sin(\omega t)$, $\kappa = 0.072$, using the $\gamma - Re_\theta$ transition model. Red Cross: Transition model-Upstroke, Blue cross: Transition model-downstroke, Red circles: Experiment-upstroke, Blue circles: Experiment-downstroke.

predictions with the experimental data for the *clean* airfoil oscillating as $\alpha(t) = 12^0 + 8^0 sin(\omega t)$, $\kappa = 0.1$. In this case, the maximum AoA reached is $\approx 4^0$ beyond the experimental static stall AoA. From the variation of c_l with AoA (Fig. 18(a)), a delay in stall prediction as well a significantly less *DOH* can be observed as compared to the experiment. This predicted deviation from the experiment is related to the delayed separation and stall observed in the static case. This discrepancy is not so prominent in the previous *deep stall* case ($\alpha(t) = 15^0 + 10^0 sin(\omega t)$, $\kappa = 0.1$), because the maximum AoA reached is far greater than AoA corresponding to static stall, so there is sufficient variation in AoA to predict flow separation and vortex formation before inception of the downstroke. As a result, force and moment coefficients are well predicted during the downstroke with reattachment. For this case, because flow separation on the suction side does not develop completely during the upstroke, c_l is over-predicted with accompanying under-prediction of c_d at the higher angles of attack.

For the other case with $\alpha(t) = 10^0 + 6^0 sin(\omega t)$, $k = 0.072$ similar observations can be made for

the transition model predictions (Fig. 19). The extent of hysteresis is under-predicted accompanied by over-predictiona and under-prediction of c_l and c_d at the higher AoA's. Also, in this *stall onset* case, from the experimental dataset, it can be observed that there is a sharp decrease in the lift coefficient at the maximum angle of attack. While this phenomenon can be explained for cases where significant leading edge vortex shedding is present, its occurrence for this particular *light stall* case can be possibly attributed to experimental errors.

So in both of these cases, where the maximum AoA is not well beyond the angle of attack corresponding to static stall, the $\gamma - Re_\theta$ transition model performs poorly in predicting the overall boundary layer dynamics. This may be linked to the spurious delayed prediction of static stall.

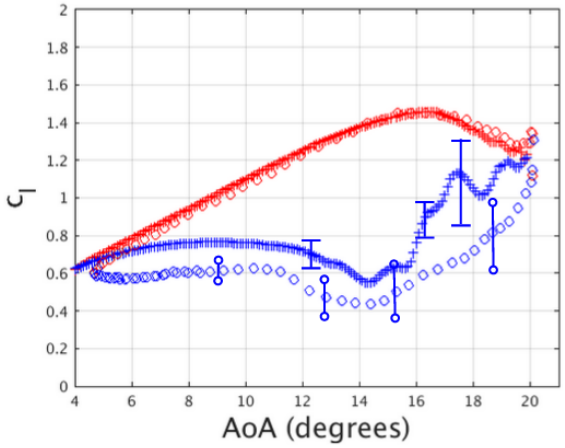

(a) Coefficient of lift (c_l)

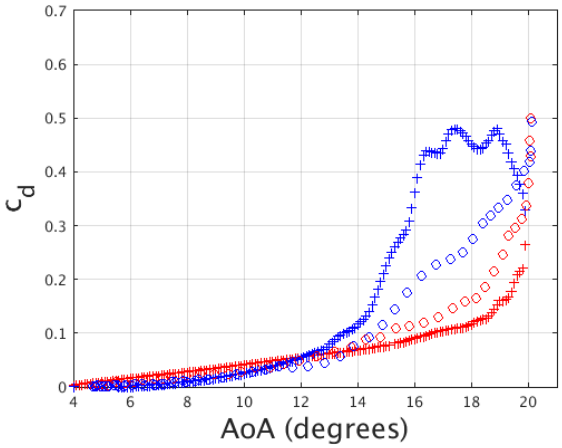

(b) Coefficient of drag (c_d)

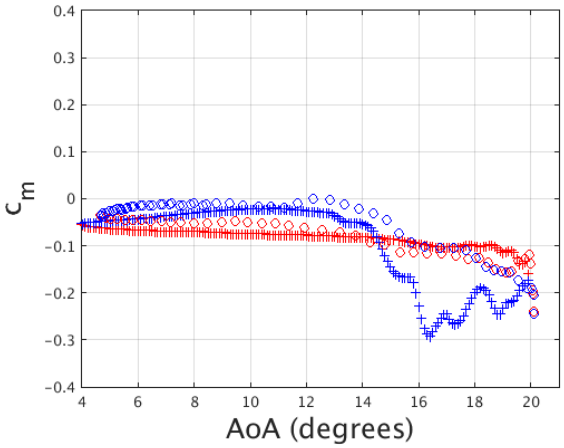

(c) Coefficient of moment (c_m)

Figure 20: Variation of lift, drag and moment coefficient predictions with AoA after scaling the AoA range (according to Coder et al.[33]) for $\alpha(t) = 12^0 + 8^0 sin(\omega t)$, $\kappa = 0.01$, using the $\gamma - Re_\theta$ transition model. Red Cross: Transition model-Upstroke, Blue cross: Transition model-downstroke, Red circles: Experiment-upstroke, Blue circles: Experiment-downstroke.

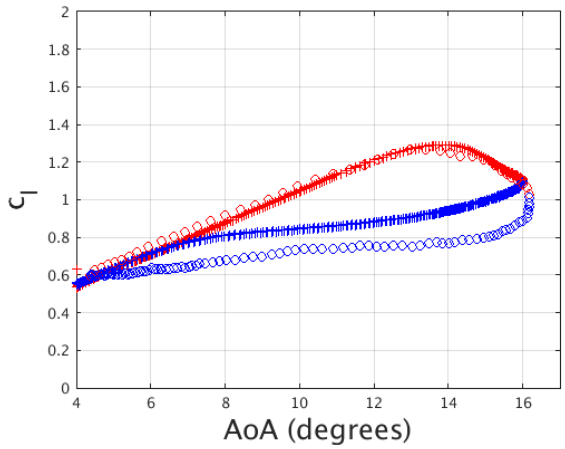

(a) Coefficient of lift (c_l)

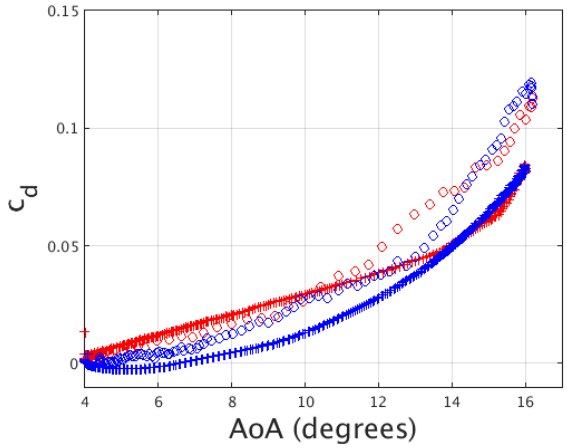

(b) Coefficient of drag (c_d)

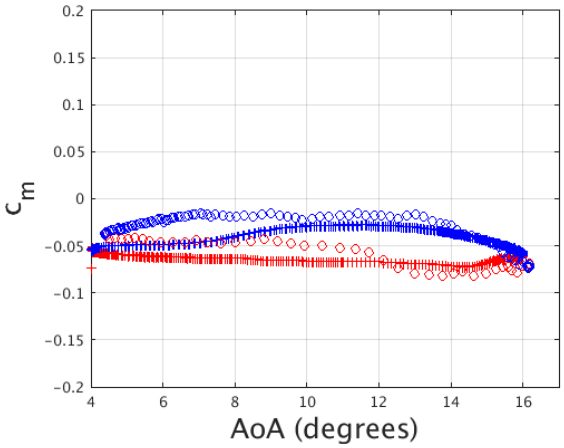

(c) Coefficient of moment (c_m)

Figure 21: Variation of lift, drag and moment coefficient predictions with AoA after scaling the AoA range (according to Coder et al.[33]) for $\alpha(t) = 10^0 + 6^0 sin(\omega t)$, $\kappa = 0.072$, using the $\gamma - Re_\theta$ transition model. Red Cross: Transition model-Upstroke, Blue cross: Transition model-downstroke, Red circles: Experiment-upstroke, Blue circles: Experiment-downstroke

(b) **Scaling of the AoA range[33] to improve predictions**

Coder et al.[33] proposed a scaling of the AoA range for the oscillating airfoil simulations to better predict physics similar to those from the experiment, based on the recognition that RANS based models commonly incorrectly predict delayed stall even for static airfoils. Assuming that the physics is otherwise correctly predicted in nonsteady flow, they adjusted the mean and amplitude of oscillation based on the deviation of the model predictions for the static airfoil from the corresponding experimental data. When this adjustment is applied to the latter two cases, the discrepancy between the transition model predictions and experiments significantly reduced as shown in Figs. 20 and 21. Separation and stall are much better predicted leading to much better prediction of the hysteresis behavior in c_l and better predictions of the force coefficients at the higher angles of attack.

VII. Conclusions

In this study the nonsteady aerodynamic environment experienced by MW level wind turbine blade sections is estimated from CFD[24] and BEM[25] studies of a NREL 5MW wind turbine rotor. It is observed that blade sections from the root to around 50% span experience nonsteady aerodynamics. Two-dimensional CFD simulations using the SST turbulence model and the $\gamma - Re_\theta$ transition model are carried out to assess their ability to predict the boundary layer dynamics of an oscillating S809 airfoil experiencing similar nonsteady environment.

Results from the study indicate that the $\gamma - Re_\theta$ transition model performs better than the fully turbulent SST model in capturing the static lift curve from the *clean* airfoil experiments, particularly near stall, albeit with delayed stall prediction accompanied by over-prediction of lift. The prediction of the nonsteady loads on the oscillating S809 airfoil is quite challenging due to it's complicated stall onset behavior.[31] From our study it can be stated that, for *deep stall*, where the maximum AoA reached by the airfoil (α_{max}) far exceeds the static stall AoA, the transition model predicts the boundary layer events observed in the experiment[1] better than the SST turbulence model. This improvement in prediction by the transition model can be attributed to it's ability to predict the laminar region near the leading edge at high angles of attack, promoting the growth of instabilities which finally lead to the formation of the leading edge vortex. For *stall onset* and *light stall*, where the maximum AoA reached during oscillation is comparable or slightly larger than the static stall AoA, the predictions from the transition model are not staisfactory. This observation stems from the fact that the model perform poorly near and beyond stall for static airfoil, under-predicting the extent of separated flow. Scaling of the AoA range for these cases as suggested by Coder et al.[33] significantly improved the transition model predictions.

Acknowledgements

We are grateful to Drs. Wanan Sheng and Frank Coton for providing us the data from the University of Glasgow experiments and addressing all the queries we had. This work was supported through the Department of Energy Offshore wind program. We would also like to acknowledge the National Science Foundation for providing the computational resources through the XSEDE program.

References

[1]W. Sheng, R. A. M. Galbraith, F. N. Coton, and R. Gilmour, "The collected data for tests on an S809 aerofoil," tech. rep., Department of Aerospace Engineering, University of Glasgow, 2006.

[2]A. W. Lavely, G. Vijayakumar, M. P. Kinzel, J. G. Brasseur, and E. G. Paterson, "Space-time loadings on wind turbine blades driven by atmospheric boundary layer turbulence," *49th AIAA Aerospace Sciences Meeting including the New Horizons Forum and Aerospace Exposition*, 2011.

[3]W. McCroskey, "Unsteady airfoils," *Annual Review of Fluid Mechanics*, vol. 14, no. 3, pp. 285–311, 1982.

[4]W. McCroskey, K. McAlister, L. Carr, S. Pucci, O. Lambert, and R. Indergrand, "Dynamic stall on advanced airfoil sections," *Journal of the American Helicopter Society*, vol. 26, no. 3, pp. 40–50, 1981.

[5]K. W. McAlister, L. W. Carr, and W. J. McCroskey, "Dynamic stall experiments on the NACA 0012 airfoil," 1978.

[6]J. Leishman, "Dynamic stall experiments on the NACA 23012 aerofoil," *Experiments in Fluids*, vol. 9, no. 1-2, pp. 49–58, 1990.

[7]J. Martin, R. Empey, W. McCroskey, and F. Caradonna, "An experimental analysis of dynamic stall on an oscillating airfoil," *Journal of the American Helicopter Society*, vol. 19, no. 1, pp. 26–32, 1974.

[8]W. Geissler and H. Haselmeyer, "Investigation of dynamic stall onset," *Aerospace science and technology*, vol. 10, no. 7, pp. 590–600, 2006.

[9]P. Wernert, W. Geissler, M. Raffel, and J. Kompenhans, "Experimental and numerical investigations of dynamic stall on a pitching airfoil," *AIAA journal*, vol. 34, no. 5, pp. 982–989, 1996.

[10]R. R. Ramsay, H. M. J, and G. G. M, "Effects of grit roughness and pitch oscillations on the S809 airfoil," tech. rep., NREL, 1999.

[11]T. Lee and P. Gerontakos, "Investigation of flow over an oscillating airfoil," *Journal of Fluid Mechanics*, vol. 512, pp. 313–341, 2004.

[12]L. W. Carr and M. Chandrasekhara, "Compressibility effects on dynamic stall," *Progress in Aerospace Sciences*, vol. 32, no. 6, pp. 523–573, 1996.

[13]N. N. Sørensen, "CFD modelling of laminar-turbulent transition for airfoils and rotors using the $\gamma - Re_\theta$ model," *Wind Energy*, vol. 12, no. 8, pp. 715–733, 2009.

[14]R. B. Langtry and F. R. Menter, "Correlation-based transition modeling for unstructured parallelized computational fluid dynamics codes," *AIAA journal*, vol. 47, no. 12, pp. 2894–2906, 2009.

[15]J. Counsil and K. Goni Boulama, "Validating the URANS shear stress transport γ-Re$_\theta$ model for low-reynolds-number external aerodynamics," *International Journal for Numerical Methods in Fluids*, vol. 69, no. 8, pp. 1411–1432, 2012.

[16]T. Rinehart, S. Medida, S. Thomas, and J. D. Baeder, "Computation of two-dimensional wind turbine airfoil characteristics using advanced turbulence and transition modeling methods and a GPU-accelerated Navier-Stokes solver," in *AIAA Scitech*, 2014.

[17]R. R. Brodeur and C. Van Dam, "Transition prediction for a two-dimensional Reynolds Averaged Navier Stokes method applied to wind turbine airfoils," *Wind Energy*, vol. 4, no. 2, pp. 61–75, 2001.

[18]V. Gleize, M. Costes, A. Le Pape, and F. Richez, "Numerical simulation of a pitching airfoil under dynamic stall conditions including laminar/turbulent transition," in *46th AIAA Aerospace Sciences Meeting*, 2008.

[19]S. Wang, D. B. Ingham, L. Ma, M. Pourkashanian, and Z. Tao, "Numerical investigations on dynamic stall of low Reynolds number flow around oscillating airfoils," *Computers & Fluids*, vol. 39, no. 9, pp. 1529–1541, 2010.

[20]S. Medida and J. Baeder, "Numerical prediction of static and dynamic stall phenomena using the $\gamma - Re_{\theta t}$ transition model," in *American Helicopter Society 67th Annual Forum*, 2011.

[21]K. Richter, A. Le Pape, T. Knopp, M. Costes, V. Gleize, and A. Gardner, "Improved two-dimensional dynamic stall prediction with structured and hybrid numerical methods," *Journal of the American Helicopter Society*, vol. 56, no. 4, pp. 1–12, 2011.

[22]B. A. Vieira and M. D. Maughmer, "An evaluation of dynamic stall onset prediction methods for rotorcraft airfoil design," in *51st AIAA Aerospace Sciences Meeting Including the New Horizons Forum and Aerospace Exposition*, 2013.

[23]J. Howison and K. Ekici, "Dynamic stall analysis using harmonic balance and correlation-based $\gamma - Re_{\theta t}$ transition models for wind turbine applications," *Wind Energy*, vol. 18, pp. 2047–2063, 2015.

[24]G. Vijayakumar, A. W. Lavely, B. Jayaraman, B. C. Craven, and J. G. Brasseur, "Blade boundary layer response to atmospheric boundary layer turbulence on a NREL 5MW wind turbine blade with hybrid URANS-LES," *AIAA SciTech*, 2014.

[25]A. W. Lavely ,*Private communication*, 2015.

[26]T. Corke and F. Thomas, "Dynamic stall in pitching airfoils: Aerodynamic damping and compressibility effects," *Annual Review of Fluid Mechanics*, vol. 47, pp. 479–505, 2015.

[27]F. R. Menter, "Two-equation eddy-viscosity turbulence models for engineering applications," *AIAA journal*, vol. 32, no. 8, pp. 1598–1605, 1994.

[28]"OpenFOAM: The open source CFD toolbox," tech. rep., OpenFOAM Foundation Ltd., year = 2011,.

[29]D. Somers, "Design and experimental results tor the S809 airfoil," tech. rep., SR-440-6918, National Renewable Energy Laboratory, 1997.

[30]J. G. Leishman, "Challenges in modelling the unsteady aerodynamics of wind turbines," *Wind Energy*, vol. 5, no. 2-3, pp. 85–132, 2002.

[31]W. Sheng, R. A. M. Galbraith, and F. N. Coton, "On the S809 airfoil's unsteady aerodynamic characteristics," *Wind Energy*, vol. 12, no. 8, pp. 752–767, 2009.

[32]K. Standish, P. Rimmington, J. Laursen, and H. N. Paulsen, "Computational prediction of airfoil roughness sensistivity," in *48th AIAA Aerospace Sciences Meeting including the New Horizons Forum and Aerospace Exposition*, 2010.

[33]J. G. Coder, M. D. Maughmer, and M. Preston, "CFD investigation of unsteady rotorcraft airfoil aerodynamics: Mites and dynamic stall," in *49th AIAA Aerospace Sciences Meeting including the New Horizons Forum and Aerospace Exposition*, 2011.